Universiteit Leiden
The Netherlands

Origami metamaterials : design, symmetries, and combinatorics
Dieleman, P.

Citation
Dieleman, P. (2018, October 16). *Origami metamaterials : design, symmetries, and combinatorics*. *Casimir PhD Series*. Retrieved from https://hdl.handle.net/1887/66267

Version: Not Applicable (or Unknown)
License: Licence agreement concerning inclusion of doctoral thesis in the Institutional Repository of the University of Leiden
Downloaded from: https://hdl.handle.net/1887/66267

Note: To cite this publication please use the final published version (if applicable).

Cover Page

Universiteit Leiden

Leiden University Repository

The handle http://hdl.handle.net/1887/66267 holds various files of this Leiden University dissertation.

Author: Dieleman, P.

Title: Origami metamaterials : design, symmetries, and combinatorics

Issue Date: 2018-10-16

CHAPTER 5

MULTISTABILITY OF NON-FLAT VERTICES

5.1 Introduction

One appealing feature of many origami patterns is that they readily exhibit multistable behavior. For example: a simple waterbomb pattern, consisting of folds of alternating sign coming together at a vertex is generically bistable [66, 67]. Here the flexibility of the folds and the flexibility of the material work together to create one stable shape at zero elastic energy, and one stable shape at finite energy. Other examples of bistability also exploit the finite stiffness of the plate material to achieve bistable structures [68, 69], whereas yet other studies focus on strictly rigid folding structures dressed by linear or torsional springs [28, 34, 70, 71]. Both of these approaches however, generally consider only bistable behavior [28, 34, 66, 67, 70].

A Euclidean 4-vertex which is made out of paper –or any other flat material– has two folding branches, which connect at the flat state [28]. As a consequence, when one of the fold angles is fixed, the vertex can be in two distinct configurations. It is therefore straightforward to make a bistable element out of a 4-vertex mechanism, by putting a single torsional spring on any of the four folds. When additionally putting springs on the three remaining folds, it is theoretically possible to create tri-, quad-, penta-, and hexa-stable vertices [28]. However, these more complex energy landscapes only occur in a small region of the phase space spanned by the sector angles of the vertex and the spring rest angles and stiffnesses. Moreover, most of the energy minima are shallow. It is therefore difficult to turn these designs into actual tri-stable vertices.

In this chapter we aim to create experimentally robust *tristable* 4-vertices. To do so, we opt for a novel approach, based on non-flat, non-Euclidean 4-vertices. For these, the sum of sector angles $\sum \alpha_i$ is unequal to 2π. Such non-flat vertices occur in non-developable origami structures, which typically consist of cells which are glued together, such as eggbox patterns [72], tubular origami structures [54], as well as 3D-origami stackings [26].

For a non-Euclidean vertex, the flat state is no longer accessible by rigidly folding the vertex. As a consequence, the two folding branches split apart [73], as we discuss below, and the only way to switch from one branch to another is by 'popping through' the vertex. This branch splitting will be harnessed to create a vertex with two global ($E = 0$) minima on one folding branch, and one additional *local* minimum ($E > 0$) on the other folding branch.

In this chapter we experimentally demonstrate these tristable vertices. In section 5.2 we explain the theory behind non-flat 4-vertices, and under which conditions they are tristable. In section 5.3 we show how we fabricate the vertices by means of 3D printing, as well as our experimental setup. In section 5.4 we show our results. Based on these experiments, we calculate energy curves, which show clear tristable behavior. We compare these to our theoretical predictions in section 5.4.4 and find good agreement. Hence we present a generic and robust route to fabricate tristable vertices.

5.2 Non-Flat 4-Vertices

In this section we will show how the two branches of a flat 4-vertex separate when the four sector angles of the vertex add up to slightly less, or slightly more, than 2π. The separation of the two folding branches effectively creates an energy barrier between the two folding branches, which we harness to design tristable 4-vertices.

5.2.1 Phenomenology

In order to understand the folding behavior of a non-flat vertex, we first consider the two folding branches of a flat vertex. In Fig. 5.1.A we show a flat 4-vertex with sector angles α_i for a vertex with sector angles $\alpha_i = \{\pi/3, \pi/2, 3\pi/4, 5\pi/12\}$ for $i = 1, 2, 3, 4$, which is the same geometry as the vertex in Fig. 5.1.A. When we fold this 4-vertex it can be modeled as a mechanism which has a single continuous degree of freedom, and two folding branches that meet in the flat state. Spherical trigonometry can be used to derive the relationships $\rho_i(\rho_j)$ on the two principal folding branches, which we name branch-I and branch-II. On branch I, the sign of ρ_4 is opposite to all others, whereas on the branch II the sign of ρ_1 is opposite to all others. These two folds, ρ_4 and ρ_1 are so called 'odd-folds', which are found on either side of the 'odd plate', which is defined as the plate for which the corresponding sector angle satisfies [28],

$$\alpha_i + \alpha_{i+1} < \alpha_{i+2} + \alpha_{i+3}, \tag{5.1}$$

$$\alpha_i + \alpha_{i+3} < \alpha_{i+1} + \alpha_{i+2}. \tag{5.2}$$

We further subdivide these in branches I^+ and II^+, for which three out of the four folds are positive in sign, as well as I^- and II^-, for which three out of the four folds are negative in sign. In Fig. 5.2.A we plot the relationships $\rho_i(\rho_1)$.

From the folding branches in Fig. 5.2.A it is evident that putting a torsional spring on any of the four folds ρ_i results in a bistable vertex. A

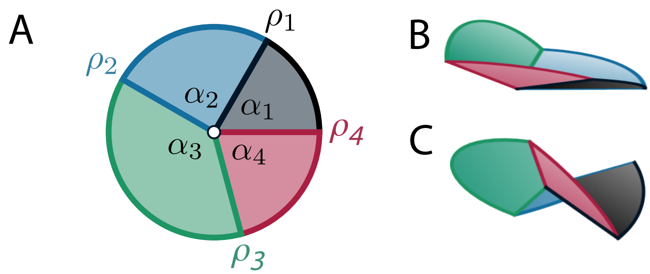

FIGURE 5.1: (A) Flat 4-vertex with sector angles $\alpha_i = \{\pi/3, \pi/2, 3\pi/4, 5\pi/12\}$ (B) Vertex where the α_i of A are uniformly shrunk by a factor $f < 1$ ($\alpha_i' = f \cdot \alpha_i$) such that $\sum \alpha_i < 2\pi$. As depicted, this vertex has assumed a 'hat-shape', where all the ρ_i are identical in sign, which is not possible with flat vertices. **C:** Vertex where the α_i of A are uniformly expanded by a factor $f > 1$ such that $\sum \alpha_i > 2\pi$. As depicted, this vertex has assumed a 'saddle-shape' where the ρ_i alternate in sign. This alternation is not possible with flat vertices. Figure from [74].

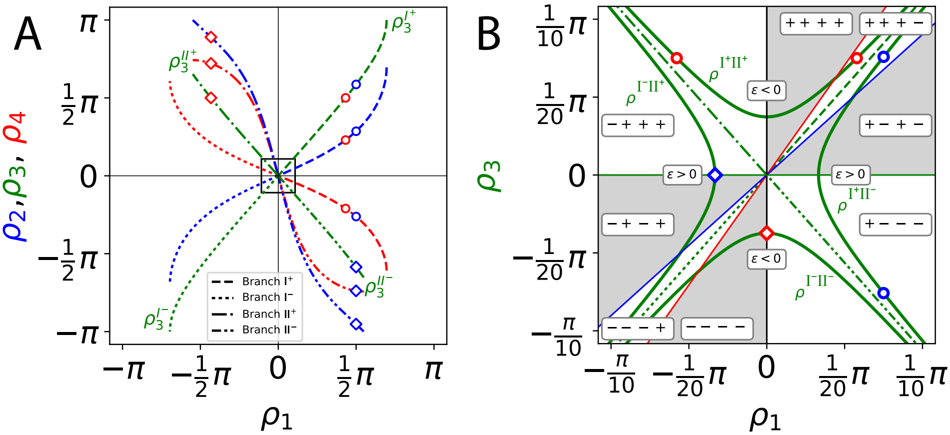

FIGURE 5.2: (A) Folding branches $\rho_i^{I^+}(\rho_1)$, $\rho_i^{I^-}(\rho_1)$, $\rho_i^{II^+}(\rho_1)$, and $\rho_i^{II^-}(\rho_1)$ for $i = 2, 3, 4$, for a flat vertex with sector angles as in Fig. 5.1.A. (B) Plot of ρ_3 as a function of ρ_1 for the small area around the origin shown in A. The dashed, and double dashed lines through the origin correspond to $\rho_3^{I^{+/-}}(\rho_1)$ and $\rho_3^{II^{+/-}}(\rho_1)$ as in A, for $\epsilon = 0$. The curved green lines indicate the merged folding branches $\rho^{I^-II^+}$ and $\rho^{I^+II^-}$ (for $\epsilon > 0$), and $\rho^{I^+II^+}$ and $\rho^{I^-II^-}$ (for $\epsilon < 0$). The solid black, blue, green, and red lines indicate where the folding angles ρ_1, ρ_2, ρ_3, and ρ_4 change sign, and divide the plot in eight sectors, with the signs of their fold angles as indicated.

spring with rest angle ϕ placed on fold i results in stable states with $\rho_i = \phi$, of which there are always two, provided $\phi \neq 0$ and ϕ is not too large (not all ρ_i reach $\pm\pi$ along their folding branches). We show two specific examples. First, we consider a torsional spring with a positive rest angle $\rho_{\text{spring}} = \pi/2$ on the ρ_1 fold. As this single spring wants to relax to its rest angle, this results in two stable configurations: one on the I^+ branch, and one the II^- branch. The blue dots (for branch I^+) and blue diamonds (for branch II^-) at $\rho_1 = \rho_{\text{spring}}$ on these two branches indicate the ρ_i values for the two equilibrium configurations. Second, when we choose to put the same torsional spring on ρ_3, we again find two stable states: one on the I^+ branch as before, and one on the II^+ branch. Here the red dots (for branch I^+) and red diamonds (for branch II^+) on these two branches indicate the two equilibrium configurations for which $\rho_3 = \rho_{\text{spring}}$. For convenience, we summarize the signs of the folding angles on the four different branches in table 5.1. From this, we deduce that a single spring on one of the two odd

	ρ_1	ρ_2	ρ_3	ρ_4
I^+	$+$	$+$	$+$	$-$
I^-	$-$	$-$	$-$	$+$
II^+	$-$	$+$	$+$	$+$
II^-	$+$	$-$	$-$	$-$

TABLE 5.1: Overview of the signs of the folding angles on the four $\epsilon = 0$ folding branches.

folds yields stable states at branch I^+II^- or I^-II^+; a single spring on one of the other folds yields stable states at branch I^+II^+ or I^-II^-.

This picture changes completely when we uniformly shrink or expand all the sector angles α_i by a factor f, such that the vertex is no longer euclidean. To describe these vertices we define the surplus angle, $\epsilon = f\sum\alpha_i - 2\pi$. Here $\epsilon < 0$, $f < 1$, corresponds to a vertex for which $\sum\alpha_i < 2\pi$, which results in a hat shaped vertex, as depicted in Fig. 5.1.B. Conversely, $\epsilon > 0$, $f > 1$, corresponds to a vertex for which $\sum\alpha_i > 2\pi$, which results in a saddle shaped vertex, as depicted in Fig. 5.1.C. For a flat vertex, where $\epsilon = 0$, the branching point of the two branches I and II is the flat state, where all $\rho_i = 0$. For a vertex where $\epsilon \neq 0$ this branching point disappears, resulting in disjoint folding branches.

We now explain what happens to the folding branches for $\epsilon \neq 0$, by focusing on the relation $\rho_3(\rho_1)$ in the area around the origin corresponding to the black square in Fig. 5.2.A, shown in large in Fig. 5.2.B[1]. Here the four curves $\rho_3^{I^+}(\rho_1)$, $\rho_3^{I^-}(\rho_1)$, $\rho_3^{II^+}(\rho_1)$, and $\rho_3^{II^-}(\rho_1)$ for $\epsilon = 0$ are shown by the four green lines meeting at the origin. When we introduce a small angular offset, such that $\epsilon \neq 0$, we find that for $\epsilon < 0$ the two branches I^+ and II^+ merge together. This creates a new folding branch, which we shall indicate by I^+II^+. In Fig. 5.2.B this corresponds to the $\rho_3^{I^+II^+}(\rho_1)$ curve. Similarly, we find that for $\epsilon < 0$ and $\rho_3 < 0$, the two branches $\rho_3^{I^-}(\rho_1)$ and $\rho_3^{II^-}(\rho_1)$ merge to form $\rho_3^{I^-II^-}(\rho_1)$. We note that for $\epsilon < 0$, the signs of the fold angles ρ_i vary as $(+++-) \mapsto (++++) \mapsto (-+++)$ or ρ_i as $(---+) \mapsto (----) \mapsto (+---)$. Hence, these vertices can form a 'cone' $(++++)$, or 'bowl' $(+---)$ shape (see Table 5.2).

For the $\epsilon > 0$ case we find that the branches $\rho_3^{I^-}(\rho_1)$ and $\rho_3^{II^+}(\rho_1)$ merge to form $\rho_3^{I^-II^+}(\rho_1)$ when $\rho_1 < 0$. For $\epsilon > 0$ and $\rho_1 > 0$ we find that $\rho_3^{I^+}(\rho_1)$

[1] We here explicitly calculated the branches, but this scenario is generic [74].

and $\rho_3^{II^-}(\rho_1)$ merge to form $\rho_3^{I^+II^-}(\rho_1)$. Along these branches, the signs of the fold angles vary as $(- - -+) \mapsto (- + -+) \mapsto (- + ++)$, or as $(+ + +-) \mapsto (+ - +-) \mapsto (+ - --)$. Hence, these vertices can form a 'saddle' $(+ - +-)$ or $(- + -+)$ shape (see Table 5.2). As illustrated in Fig. 5.2 there are still two possible folding branches for both $\epsilon > 0$ and $\epsilon < 0$. However, they are no longer connected by a common branching point.

		ρ_1	ρ_2	ρ_3	ρ_4
$\epsilon < 0$	I^+II^+	$+$	$+$	$+$	$-$
		$+$	$+$	$+$	$+$
		$-$	$+$	$+$	$+$
	I^-II^-	$-$	$-$	$-$	$+$
		$-$	$-$	$-$	$-$
		$+$	$-$	$-$	$-$
$\epsilon > 0$	I^-II^+	$+$	$+$	$+$	$-$
		$+$	$-$	$+$	$-$
		$+$	$-$	$-$	$-$
	I^+II^-	$-$	$-$	$-$	$+$
		$-$	$+$	$-$	$+$
		$-$	$+$	$+$	$+$

TABLE 5.2: Overview of the signs of the folding angles on the four folding branches for $\epsilon \neq 0$.

In this chapter we will harness the disconnectedness of the two folding branches for $\epsilon \neq 0$ to create tristable origami vertices. For example, the separation of the $\rho_3^{I^-II^-}$ and the $\rho_3^{I^+II^+}$ branches in the $\epsilon < 0$ case means that we can not change the sign of ρ_3 by rigid folding. However, real vertices have finite stiffness, and can be elastically deformed, by bending and stretching the plates and hinges. This enables us to 'pop-through' the vertex from branch $\rho_3^{I^+II^+}$ to $\rho_3^{I^-II^-}$ or vice versa. The angular surplus ϵ effectively creates an energy barrier between a cone with folding angles $- - --$, and a cone with folding angles $+ + ++$. Similarly, the $\epsilon > 0$ case exhibits a saddle-to-saddle transition when popping the vertex through such that we force the vertex from the folding branch $\rho_3^{I^+II^-}$, with sign configuration $- + -+$, into folding branch $\rho_3^{I^-II^+}$ with sign configuration $+ - +-$.

We now show that a vertex with an angular offset $|\epsilon| > 0$, combined with a single torsional spring, allows us to make a tristable vertices. To demonstrate this, imagine attaching a single torsional spring with a rest angle of $\rho_{\text{spring}} = 3\pi/40$ on the ρ_1 fold of a $\epsilon > 0$ vertex. As we can see in Fig. 5.2.B, this results in two stable ($E = 0$) configurations on the $\rho_3^{I^+II^-}$ branch, one where $\rho_3 > 0$, and one where $\rho_3 < 0$, indicated by the blue dots. When we pop this vertex through to the folding branch $\rho_3^{I^-II^+}$, one additional *local* minimum can be found on the $\rho_3^{I^-II^+}$ branch, indicated by the blue diamond. Here $E \neq 0$, as the spring cannot reach its relaxed state, as the torsional spring wants to minimize its energy, the energy minimum is located as close to $\rho_1 = \rho_{\text{spring}}$ as possible. This minimum, which is not present when $\epsilon = 0$, is stable provided that the energy necessary to 'pop-through' the vertex from the I^-II^+ branch to the I^+II^- is sufficiently high compared to the energy stored in the spring. Conversely, we can make a tristable $\epsilon < 0$ vertex by putting a $\rho_{\text{spring}} = 3\pi/40$ on the ρ_3 fold. In Fig. 5.2.B we see this results in two stable states on the $\rho_3^{I^+II^+}$ folding branch, as indicated by the two red dots. A third, local minimum can be found on the $\rho_3^{I^-II^-}$ folding branch when we pop the vertex through from the I^+II^+ branch to the I^-II^- branch, as is indicated by the red diamond.

Inspecting the signs of the fold angles on the $\epsilon \neq 0$ branches as summarized in table table 5.2, as well as the generic sketch of these branches in Fig. 5.2, we conclude that $\epsilon < 0$ vertices can be made tristable by putting a single spring on ρ_2 or ρ_3, i.e. a fold opposite to the odd folds (ρ_4, ρ_1) of the corresponding flat vertex. On the contrary, $\epsilon > 0$ vertices can be made tristable by putting a single spring on one of the two odd folds of the corresponding flat vertex.

5.2.2 Theoretical Energy Curves

In this section we compute the elastic energy as a function of fold angle, for non-Euclidean 4-vertices, augmented with a single torsional spring. We focus on the scenarios outlined in the previous section that potentially lead to tristable vertices. We consider vertices with sector angles $\alpha_i = (1 + \frac{\epsilon}{2\pi})\{\pi/3, \pi/2, 3\pi/4, 5\pi/12\}$, and angular surplus of $\epsilon = \sum \alpha_i - 2\pi = \pm\{0.001, 0.01, 0.03, 0.001\}$ rad.

For the cone-like, $\epsilon < 0$ vertices we choose to put the spring on the ρ_4 fold of the vertices. As discussed in the previous section this leads to two stable states on the I^+II^+ branch, and one stable state on the I^-II^-

branch. Assuming a torsional spring with a stiffness k_{spring}, and a rest angle $\rho_{spring} > 0$, the energy curves can then be calculated as,

$$E^{\epsilon<0}_{\text{bistable}}(\rho_1, \epsilon) = \frac{1}{2} \cdot k_{\text{spring}} \left(\rho_3^{I^+II^+}(\rho_1, \epsilon) - \rho_{\text{spring}} \right)^2 \tag{5.3}$$

for the bistable branch, and

$$E^{\epsilon<0}_{\text{monostable}}(\rho_1, \epsilon) = \frac{1}{2} \cdot k_{\text{spring}} \left(\rho_3^{I^-II^-}(\rho_1, \epsilon) - \rho_{\text{spring}} \right)^2 \tag{5.4}$$

for the monostable branch. The corresponding energy curves as a function ρ_1 are displayed in Fig. 5.3.A.

For the saddle-like, $\epsilon > 0$ vertices we choose to put a torsional spring on the ρ_2 fold of the vertices, which leads to one bistable branch (I^+II^-), and one monostable branch (I^-II^+), when viewed as a function of ρ_3 (see Fig. 5.2.B). The energy curves can then be calculated as,

$$E^{\epsilon>0}_{\text{bistable}}(\rho_3, \epsilon) = \frac{1}{2} \cdot k_{\text{spring}} \left(\rho_1^{I^+II^-}(\rho_3, \epsilon) - \rho_{\text{spring}} \right)^2 \tag{5.5}$$

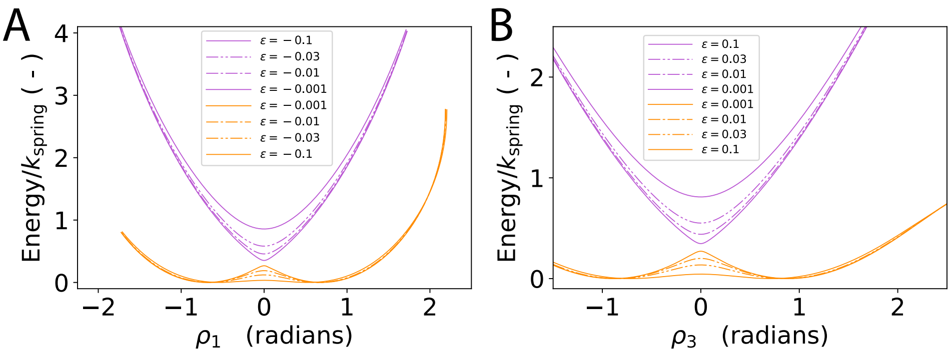

FIGURE 5.3: (A) Bistable energy curve on branch I^+II^+ (pink), and monostable energy curve on branch I^-II^- (orange), for a cone-like, $\epsilon < 0$ vertex with a spring on ρ_4, and controlling ρ_2, for various values of ϵ (see legend). (B) Bistable energy curve (pink) on branch I^+II^-, and monostable energy curve on branch I^-II^+ (orange), for a saddle-like, $\epsilon > 0$ vertex with a spring on ρ_2, and controlling ρ_4, for various values of ϵ (see legend).

and,
$$E^{\epsilon>0}_{\text{monostable}}(\rho_3, \epsilon) = \frac{1}{2} \cdot k_{\text{spring}} \left(\rho_1^{I^- II^+}(\rho_3, \epsilon) - \rho_{\text{spring}} \right)^2 \tag{5.6}$$
respectively. These energy curves are plotted in Fig. 5.3.B as function of ρ_3.

In both the $\epsilon < 0$, and the $\epsilon > 0$ case we clearly have three minima. We note that the separation of the energies at $\rho_3 = 0$ between the upper and lower branches grows as $\sqrt{\epsilon}$, which is expected for the unfolding of a transcritical scenario (the intersection of the I and II branches at $\epsilon = 0$). In addition, we notice that the depth of the two minima on the lower branch diminishes with ϵ. The experimental challenge is therefore to find a value of ϵ for which the upper and lower branch are sufficiently separated by means of the 'pop-through' barrier, but which does not wash out the two minima on the lower branch.

5.3 3D Printed Tristable Vertices

Here we describe the manufacturing of non-flat 4-vertices. Specifically, we aim to create vertices where the two branches have one, respectively two energy minima at corresponding stable states, and where the energy barrier between these branches is in the right range to allow "popping" from one branch to the other, without destroying the three energy minima on the two branches. We discuss how we make these vertices by use of 3D printing, and how we turn them into tristable vertices by dressing them with a torsional spring.

We first discuss the experimental fabrication of non-flat 4-vertices. The

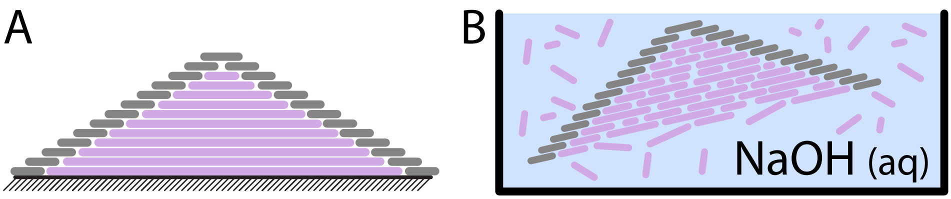

FIGURE 5.4: (A) Schematic side view of the 3D printing process, using two different materials. Vertices are built up layer by layer (in gray), and arbitrary geometries can be created by use of a scaffold material (in lilac). (B) We dissolve the scaffold in an 70° C aqueous NaOH solution, which leaves the plate material intact.

vertices we use for our experiment are 3D printed with a Stratasys Fortus 250 MC, which is capable of printing ABS plastic, as well as a sacrificial ABS-like plastic, with a layer thickness of 0.18 mm and an xy-resolution of better than 0.24 mm. The sacrificial material serves as a scaffold, and allows us to print non-flat vertices, see Fig. 5.4.A. This scaffold is subsequently dissolved by putting the structure in a 70° C sodium hydroxide (NaOH, pH 9.0) solution for 7 hours, see Fig. 5.4.B. This printing technique therefore allows us to print non-flat vertices with an arbitrary angular surplus ϵ.

We design our vertices to be 150 mm in diameter, consisting of four plates which are 3.0 mm thick, see Fig. 5.5.A. The four plates of the vertex

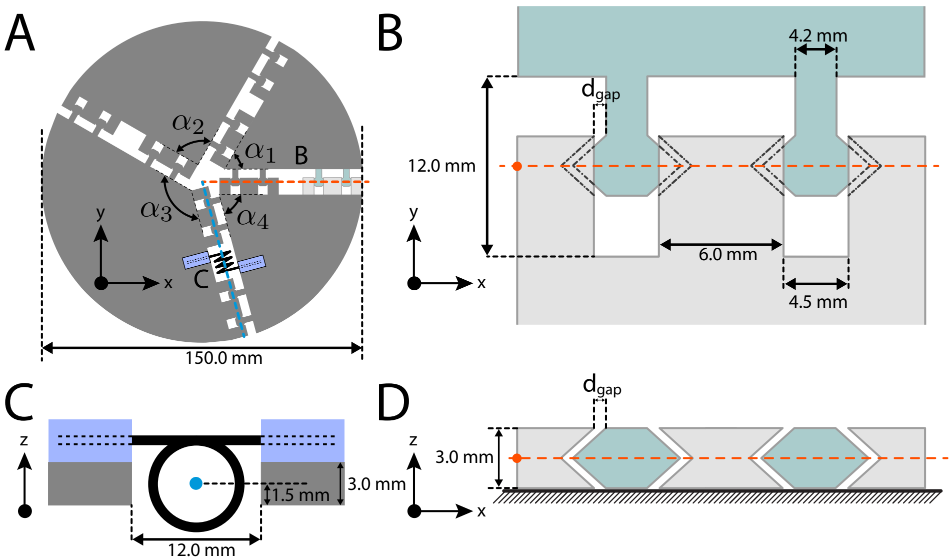

FIGURE 5.5: (A) Top view of the design of a 3D printed, (flat) 4-vertex with sector angles $\alpha_i = \{\pi/3, \pi/2, 3\pi/4, 5\pi/12\}$. This vertex is 150 mm in diameter and 3 mm thick. The plates are connected by four conically shaped hinges (detailed view in B,D). A torsional spring can be put on one of the folds (see C for a detailed side view). (B) Detailed top view of the hinges in A, where the dotted orange line indicates the axis of rotation of the conical hinges. (C) Side view of the torsional spring in A. The spring is offset from the plates of the vertex such that its axis of rotation aligns with the axis of rotation of the hinges (see blue line in B). (D) Side view cut through of the hinges in A,B. The dotted orange line indicates the axis of rotation of the conical hinges as in A,B.

are connected to each other by four hinges, and the axes of rotation of all these hinges meet at the center of the vertex. The hinges consist of two disconnected conical holes attached to one plate, and two opposing conical pins attached to the opposing plates (Fig. 5.5.B). This design allows us to closely emulate a perfect hinging fold. The main experimental limitation is the finite maximal folding angle, of approximately $|\rho_i| \approx 2.65$ rad, due to the formation of self contacts between the plates that occur for high folding angles. A detailed view of the design is shown in Fig. 5.5.B and Fig. 5.5.D. This hinge design allows us to print the vertex in its assembled state, including the hinges. However, it does require careful tuning of the d_{gap} parameter that sets the separation between the conical holes and the conical pins (Fig. 5.5.B,D). When we set d_{gap} too low, the hinges get stuck to each other after the printing process, which was found to be the case for $d_{\text{gap}} = 0.05$ mm and $d_{\text{gap}} = 0.1$ mm. Setting d_{gap} too high results in a vertex with excessive play in the hinges, which leads to significant deviations from rigid folding. The gap d_{gap} was therefore chosen to be $d_{\text{gap}} = 0.15$mm, which is roughly equal to the layer resolution of the 3D printer (at 0.18 mm).

The vertex is designed to allow to incorporate a torsional spring on one of the folds, as is shown in Fig. 5.5.A. We do this by including cylindrical holes of diameter 1.14 mm in the design of the 3D-printed vertex, which allows us to attach an Amatec T045-270-312 torsional spring. These holes are offset from the plate material such that the center of rotation aligns with that of the center of the hinges, see Fig. 5.5.C. In order to create a tristable vertex by adding a single torsional spring, we choose to print cone-like vertices such that we can attach the spring to the ρ_1 fold, and the saddle-like vertices such that we can attach the spring to the ρ_3 fold (see section5.2). Furthermore we note that the torsional springs are not irreversibly attached to the vertices, and can be taken out to perform control experiments.

For the sector angles of the vertices we choose $\alpha_i = (1 + \frac{\epsilon}{2\pi})\{\pi/3, \pi/2, 3\pi/4, 5\pi/12\}$. Our goal is to fabricate vertices which we can reversibly pop-through. This puts an upper limit on $|\epsilon|$, as the maximal stresses on the hinges during the pop-through grows with increasing $|\epsilon|$. In practice, we found that vertices for which $|\epsilon| > 0.105$ rad readily fail at the hinges after popping it through ten or less times. Conversely, vertices for which $|\epsilon| < 0.026$ rad barely show any pop-through behavior at all, presumably due to the small but finite play in the hinges. This makes such vertices unsuitable to our end goal of making tristable vertices, which requires an energy barrier between the two branches. We therefore focus on vertices with an angular surplus of $|\epsilon| = 0.052$ rad. These vertices do not break at the hinges after popping them through numerous times, yet the pop-through energy barrier of these vertices is large enough for the two folding branches to remain separated, as we will show.

5.4 Experimental Results

In this section we will first demonstrate that the 3D printed vertices of section 5.3 can be made tristable by adding a single torsional spring to one of the folds (section 5.4.1). After this, we characterize the tristable energy landscape by use of an Instron MT-1 torsion tester. We first explain the experimental protocol (section 5.4.2), then we show our experimental results (section 5.4.3), and last we convert our torsion data into experimental energy curves, in order to compare them to theoretical predictions (section 5.4.4). Finally, we show that we can control the separation between the bistable and monostable folding branches of the vertices by carefully tuning the angular surplus ϵ (section 5.4.5).

5.4.1 Tristable Vertex: Qualitative Results

In the previous section we showed that we settled on a vertex with an angular surplus of $\epsilon = \pm 0.052$ rad, which allowed for reversible pop-through behavior. To turn the 3D printed vertices into a tristable vertex, we now attach an Amatec T045-270-312 torsional spring, with a torsional stiffness of $46(1)$ mNm/rad, and rest angle $\rho_{\text{spring}} \approx 0.69(2)$. We will show that the combination of spring and vertex geometry ensures that the energy needed to pop-through the vertex, E_{pop}, is sufficiently high in comparison to the barriers of the mono- and bi-stable branches, E_{min} and E_{barrier} respectively. We can qualitatively verify that $E_{\text{min}} < E_{\text{pop}}$ by taking one of the experimentally realized vertices including the torsional spring, popping it through manually, and leaving it untouched. This is shown in Fig. 5.6.A and Fig. 5.6.D for the $\epsilon = -\pi/60 \approx -0.052$ rad and the $\epsilon = \pi/60 \approx 0.052$ rad vertex respectively. Furthermore, we can show that $E_{\text{barrier}} < E_{\text{pop}}$ by showing that the two minima on the bistable branch are stable; this is shown in Fig. 5.6.B,C and Fig. 5.6.E,F. This shows that the combination of angular surplus and torsional spring chosen here leads to a tristable vertex, both for $\epsilon < 0$ and $\epsilon > 0$.

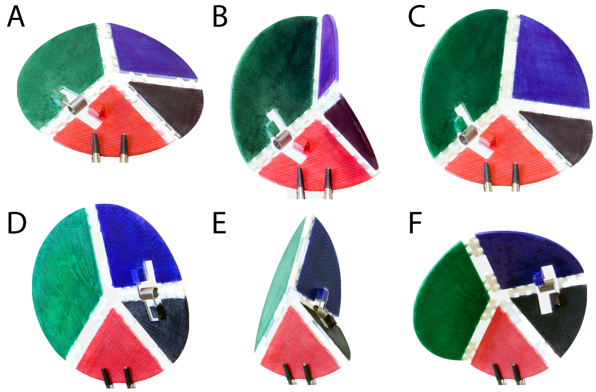

FIGURE 5.6: (A,B,C) The three stable states we found for an $\epsilon = -\pi/60$ vertex. Here (A) represents a state corresponding to a local energy minimum; (B) and (C) represent states corresponding to global energy minima, where $\rho_1 < 0$ and $\rho_1 > 0$ respectively. (D,E,F) The three stable states we found for an $\epsilon = \pi/60$ vertex. Here (D) represents a state corresponding to a local energy minimum; (E) and (F) represent states corresponding to global energy minima, where $\rho_3 < 0$ and $\rho_3 > 0$ respectively.

5.4.2 Experimental Protocol for Torsion Experiments

To quantify the multistability of these experimentally realized, non-flat 4-vertices, we aim to obtain the elastic energy as a function of one of the fold angles, on both branches, as well as the energy of the pop-through. While in principle these can be measured straight forwardly by measuring the torque as function of fold angle, in practice there are several experimental complications, due to the effect of gravity, and friction, that require special care. To measure the torque as function of fold angle, we clamp two plates of the vertex in an Instron MT-1 torsion tester with a 2.25 N·m load cell, which allows us to measure torques with an accuracy of 0.01 N·m, and angular displacement with a resolution of $5 \cdot 10^{-5}$ rad; a picture of this setup is shown in Fig. 5.7.A. In Fig. 5.7.B we depict a schematic side-view of the setup used to measure the torque as a function of the folding angle. On the left side we see the drive side of the torsion tester, which can rotate the red plate plate by means of a center-offset clamp. On the right side we see the load cell, which is stationary. In order for the load cell to measure the torque exerted on the green plate, we made a custom U-shaped clamp, which has enough clearance for the vertex to fold, and can attach on the other side of the vertex (see Fig. 5.7.B).

Protocol: (i) The first step in measuring the energy landscape of the vertex is to characterize the torsional spring by probing its spring constant k_{spring}, and rest angle ρ_{spring}. We do this by attaching the spring to the vertex and by manipulating the fold on which the spring is attached, which is fold ρ_3 for the $\epsilon < 0$ vertices, and fold ρ_1 for the $\epsilon > 0$ vertices (see section 5.3). (ii) Second, we attach the vertex differently, so as to measure the torque required to change the fold angle opposite to the spring, which is fold ρ_1 for the cone-like vertices, and fold ρ_3 for the saddle-like vertices. Here, we make sure that the vertex is on the bistable branch. (iii) Third, while the vertex is still attached to the clamps of the torsion tester, we manually force the vertex to pop-through the fold where the spring is attached, which moves the vertex to the monostable folding branch. For the cone-like vertices this means changing the sign of the ρ_3 fold from positive to negative; for the saddle-like vertices this means changing the sign of ρ_1 from positive to negative. To probe the energy landscape on the monostable branch we then measure the torque required to change fold ρ_1 for the cone-like vertices, and fold ρ_3 for the saddle-like vertices. The three torque measurements (i)-(iii) can be converted to energy landscapes by integration, and in principle yield the energy curves that can be compared to the theoretical prediction (see Fig. 5.3). However, friction and gravity also play a role, and require careful attention.

First, the hinges of the vertices are not frictionless, even though they are thoroughly sprayed with silicone oil. The resulting frictional forces show up in our measurements as an offset to the signal that we want to measure. Our approach is to "average out" the friction signal, as frictional forces are always oriented opposite to the direction of movement, and are roughly rate-independent. We therefore perform cyclic experiments, where we first increase the fold angle ρ_i to its maximum value, and then decrease ρ_i to its minimum value. For every measurement we then average the signal of the upward and downward ρ_i to suppress frictional forces. Second, even without any springs attached to the vertices, there is a non-constant torque signal due to gravitational forces. This is explained schematically in Fig. 5.7.C, and 5.7.D. As the drive shaft rotates the red plate, three of the plates change position relative to the gravitational field, which leads to a

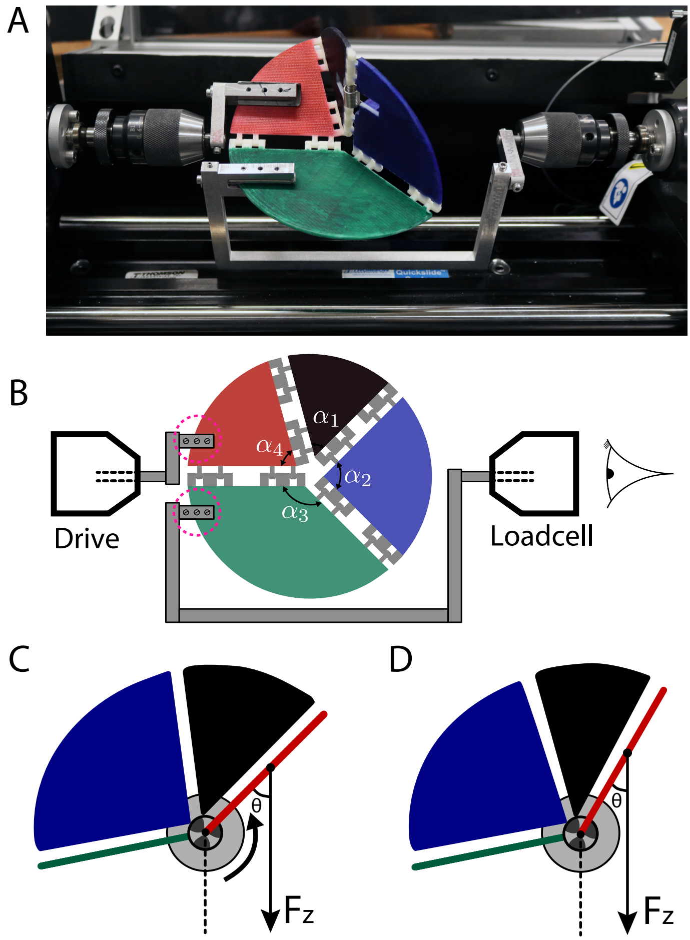

FIGURE 5.7: (A) Picture of the vertex shown in Fig. 5.6.D-F, clamped in the Instron MT-1 torsion tester. See (B) for a schematic of the setup. (B) Side view schematic of how the Instron torsion tester is connected to the 4-vertex. One plate (here plate α_4) is attached to the drive side of the tester (on the left) by means of a center-offset clamp. Another clamp is attached to the load cell side of the tester (on the right), by means of a U-shaped clamp. Note that when actuated, plates 1, 2, and 4 move, while plate 3 is kept stationary. (C,D) Cut-through schematic when looking from the side of the load cell, in the direction of the drive shaft, as indicated in panel A. The three moving plates change position in the gravitational field, which results in a non-zero torque signal, even without any spring attached to the vertex.

corresponding torque, T_{gravity}. In order to suppress this signal, we do two separate experiments: one with the torsional spring attached to the vertex, and one where we take the spring off. By subtracting these two signals, we effectively suppress the T_{gravity} signal.

By averaging the signal obtained from cyclic experiments, as well as pairing every measurement *with* spring to an identical control experiment *without* spring, we suppress both the effect of friction, as well as the effect of gravity. We therefore have to do six experiments for every vertex. Here, in summary, we list this series of experiments. First, for the cone-like vertices we perform the following six experiments:

1. manipulating ρ_3 with and without spring attached, to obtain the spring constant, k_{spring};
2. manipulating ρ_1, on the bistable branch ($\rho_3 > 0$), with and without spring attached, to probe the energy landscape of the bistable branch;
3. manipulating ρ_1, on the monostable branch ($\rho_3 < 0$), with and without spring attached, to probe the energy landscape of the monostable branch.

Likewise, for the saddle-like vertices we perform the following six experiments:

1. manipulating ρ_1 with and without spring attached, to obtain the spring constant, k_{spring};
2. manipulating ρ_3, on the bistable branch ($\rho_1 > 0$), with and without spring attached, to probe the energy landscape of the bistable branch;
3. manipulating ρ_3, on the monostable branch ($\rho_1 < 0$), with and without spring attached, to probe the energy landscape of the monostable branch.

For each of these experiments we open and close the fold that we manipulate four times, using up and down sweeps of the angle with a ramp rate of 0.070 rad/s. The maximum opening and closing angle of the fold that is manipulated is determined when the first fold reaches its maximum angle of $\rho_i \approx 2.65$ rad, at which self-contact of the hinges limits the range of movement (see previous chapter), add the aluminium clamps that are holding the plates (indicated by the two dashed circles in Fig. 5.7.B), which can contact each other.

5.4.3 Torsion Experiments - Results

We now explain in detail how we deal with gravitational and frictional forces for the measurements where we probe the torsional spring on the $\epsilon = -\pi/60$ vertex. After correcting for these spurious signals, we find that the torque exerted by the spring as function of fold angle is close to linear, which gives confidences in our methodology. We then apply the same protocol to the remaining experiments that probe the torsional spring on the $\epsilon = \pi/60$ vertex in section 5.4.3, as well as the non trivial energy landscape at each branch, in sections 5.4.3 and 5.4.3.

We now first explain in detail how we determine the spring properties by actuating the fold where the spring is attached, and how we deal with gravitational and frictional forces. We both probe the torsional spring on the $\epsilon = -\pi/60$ vertex and on the $\epsilon = \pi/60$ vertex.

Torsional Spring on a Cone-like Vertex

As explained in the above section, to determine the spring properties, we clamp the $\epsilon = -\pi/60$ vertex such that the torque is directly applied to the two plates adjacent to the spring (ρ_3 fold), and compare data with and without a spring attached. As shown in Fig. 5.8A, even without a spring attached, the raw torque signal $T_0(\rho_3)$ is complex and exhibits hysteresis. This hysteresis is due to friction, and we obtain a signal $\overline{T}_0$ by averaging over up and down sweeps (Fig. 5.8B):

$$\overline{T}_0(\rho_3) = \frac{1}{2}(T_0(\rho_3 \uparrow) + T_0(\rho_3 \downarrow)) \ . \tag{5.7}$$

As shown in Fig. 5.8C-D, we follow the same procedure for a vertex where the spring is attached, and define $\overline{T}$ as

$$\overline{T}(\rho_3) = \frac{1}{2}(T(\rho_3 \uparrow) + T(\rho_3 \downarrow)) \ . \tag{5.8}$$

After eliminating friction, the two signals $\overline{T_0}$ and $\overline{T}$ have contributions from gravity (T_g), non-rigid deformations of the vertex (T_{VD}), and in the case of $\overline{T}$, from the spring T_{spring}. The gravitational signal is expected to be very similar in $\overline{T_0}$ and $\overline{T}$, and by subtracting these signals we obtain a signal that is the sum of T_{spring} and T_{VD} (Fig. 5.9). The non-rigid deformations are due to the vertex “popping” between two branches and are the cause of the large torque spikes near $\rho_3 = 0$. The interval of the folding angles where these deformations can be expected with bounds $\pm\rho_{3,\text{min}}$ is dependent on the surplus parameter ϵ, as can be seen from Fig. 5.2.C. For the $\epsilon = -\pi/60$ vertex we find $\rho_{3,\text{min}} = \pm 0.27$ using our analytical model. Hence, for larger fold angles, the only signal is due to the spring, and indeed we observe that for $|\rho_3| > \rho_{3,\text{min}}$, the signal is essentially linear. The excellent fit to a linear function (black) indicates that the spring follows the torsional variant of Hooke's law, and can be used to extract the torsional spring constant $k_{\text{spring}} = 46(1)$ mNm/rad, as well as the rest angle: $\rho_{\text{spring}} = 0.73(1)$ rad. We conclude that, even though the raw torque signal shows large amounts of hysteresis, a significant contribution due to gravity, and near $\rho_3 = 0$ a strong signal due to vertex deformation, we can deal with these effects to characterize the torsional spring.

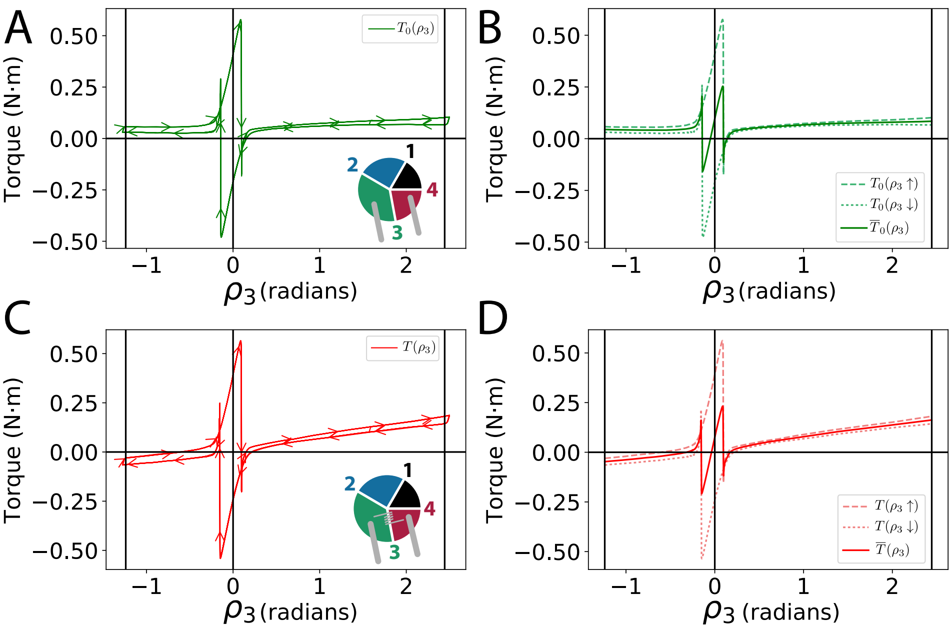

FIGURE 5.8: (A) Raw data T_0 for a measurement on a $< 2\pi$ vertex without spring attached (see inset). (B) Mean signal $\overline{T}_0$ eliminates friction but has contributions from gravity and vertex deformations. (C) Raw data T for a measurement on a $< 2\pi$ vertex with spring attached (see inset). (D) Mean signal $\overline{T}$ eliminates friction but has contributions from gravity, vertex deformations and the spring.

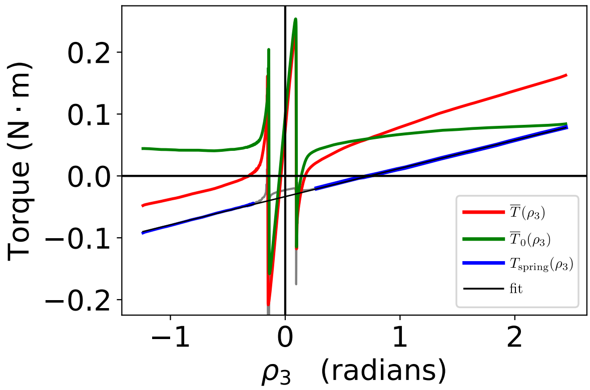

FIGURE 5.9: The difference between $\overline{T}$ and $\overline{T}_0$ is the sum of the vertex deformations, confined near $|\rho_3| < 0.27$, and a nearly linear function, due to the spring (blue). The black line indicates a linear fit.

Torsional Spring on a Saddle-like Vertex

The same experiments were performed for the $\epsilon = \pi/60$, saddle-like vertex. Here we place the spring –which is the same spring as used before– on the ρ_1 fold. The measurements *without* spring is shown in Fig. 5.10.A, and the averaged signal $\overline{T}_0(\rho_1) = \frac{1}{2}(T_0(\rho_1 \uparrow) + T_0(\rho_1 \downarrow))$ is shown in Fig. 5.10.B. The average signal of the measurement *with* spring, $\overline{T}(\rho_1) = \frac{1}{2}(T(\rho_1 \uparrow) + T(\rho_1 \downarrow))$ is shown in Fig. 5.10.D. The two signals are then subtracted, to obtain $T_{\text{spring}} = \overline{T} - \overline{T}_0$, for $|\rho_1| > \rho_{1,\text{min}}$, which is shown in Fig. 5.11. Here $\rho_{1,\text{min}} = \pm 0.25$ rad indicates the boundary within which the signal due to vertex deformations, T_{VD}, can not be neglected (see previous section).

The black line in Fig. 5.11 indicates a linear fit of the form $T_{\text{spring}} = k_{\text{spring}} \cdot (\rho_1 - \rho_{\text{spring}})$. This produces a torsional spring constant of $k_{\text{spring}} = 47(1)$ mNm/rad, which is within errorbars of the of $k_{\text{spring}} = 46(1)$ mNm/rad obtained in the previous section, as this the same identical spring. However, the rest angle seems to have changed slightly: $\rho_{\text{spring}} = 0.65(1)$ rad compared to $\rho_{\text{spring}} = 0.73(1)$ rad as extracted from the fit in Fig. 5.9. This difference in rest angle might be attributed to a slightly different way the torsional spring is glued to the vertex, resulting in a different *effective* rest angle.

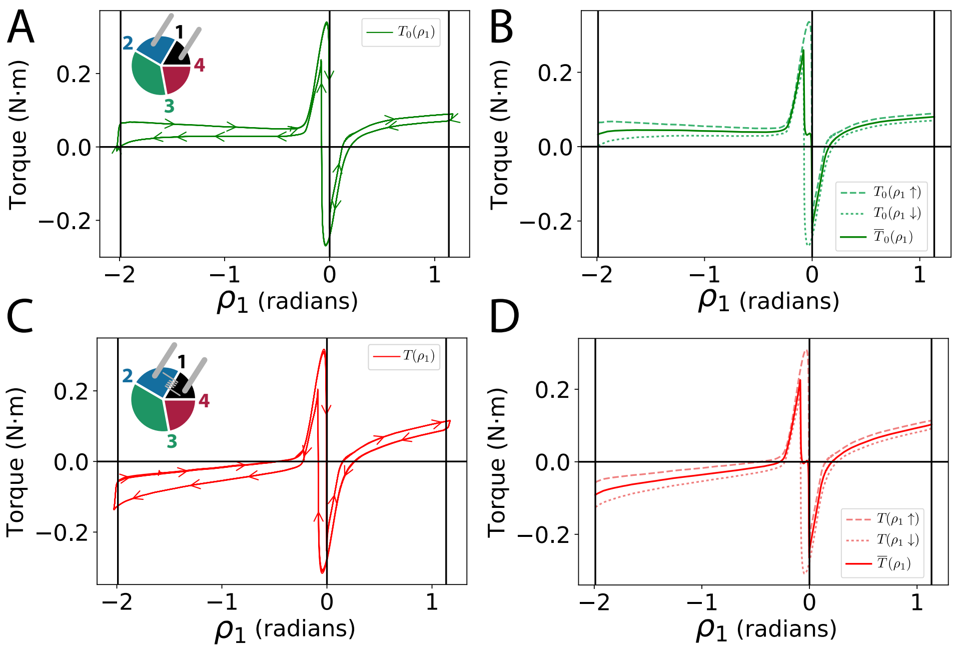

FIGURE 5.10: (A) Raw data T_0 for measurement on $> 2\pi$ vertex without spring attached (see inset). (B) Mean signal T_0 eliminates friction but has contributions from gravity and vertex deformations. (C) Raw data T for a measurement on $> 2\pi$ vertex with spring attached (see inset). (D) Mean signal $\overline{T}$ eliminates friction but has contributions from gravity, vertex deformations and the torsional spring.

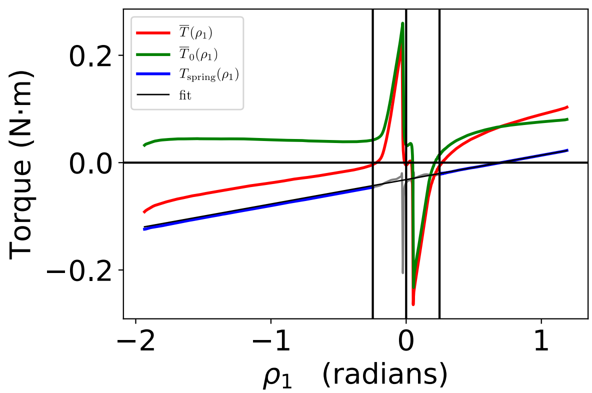

FIGURE 5.11: The difference between $\overline{T}$ and $\overline{T}_0$ is the sum of the vertex deformations, confined near $|\rho_1| < 0.25$, and a nearly linear function, due to the spring (blue). The black line indicates a linear fit.

Monostable and Bistable Branch for a Cone-like Vertex

In order to probe the bi- and monostable branch of the $\epsilon < 0$ vertex we manipulate the ρ_1 fold, with the spring on the ρ_3 fold. The sign of the ρ_3 fold then determines whether we are dealing with the bistable branch ($\rho_3 > 0$), or the monostable branch ($\rho_3 < 0$), see Fig. 5.2.C.

To extract the torque signal associated with the monostable branch, where we first need to pop the vertex through by hand such that such that $\rho_3 < 0$. After having done this, we clamp the vertex in the torsion tester such that we can manipulate the ρ_1 fold. The raw data of the measurement without spring, $T_0(\rho_1)$, is shown in Fig. 5.12.A, and the averaged signal, $\overline{T}_0(\rho_1) = \frac{1}{2}(T_0(\rho_1 \uparrow) + T_0(\rho_1 \downarrow)$, in Fig. 5.12.B. The raw data of the measurement *with* spring is displayed in Fig. 5.12.C, whereas the averaged signal $\overline{T}(\rho_1) = \frac{1}{2}(\overline{T}(\rho_1 \uparrow) + \overline{T}(\rho_1 \downarrow)$ is displayed in Fig. 5.12.D. Finally, we subtract the two signals to yield $T^{\epsilon<0}_{\mathrm{mono}}(\rho_1) = \overline{T}(\rho_1) - \overline{T}_0(\rho_1)$, which is displayed in Fig. 5.13.

The same procedure is repeated for the bistable branch –where $\rho_3 > 0$– we once again need two experiments. First, we measure *without* the spring attached, and manipulate the ρ_1 fold. The result of this measurement is shown in Fig. 5.14.A. The up and down sweeps are then averaged to suppress friction: $\overline{T}_0(\rho_1) = \frac{1}{2}(T_0(\rho_1 \uparrow) + T_0(\rho_1 \downarrow))$, see Fig. 5.14.B. Second, we measure *with* the spring on ρ_3, where the averaged torque signal $\overline{T}(\rho_1) = \frac{1}{2}(T(\rho_1 \uparrow) + T(\rho_1 \downarrow))$ is displayed in Fig. 5.14.D. Finally, we subtract the two averaged signals to find $T^{\epsilon<0}_{\mathrm{bi}}(\rho_1) = \overline{T}(\rho_1) - \overline{T}_0(\rho_1)$, which is displayed in Fig. 5.15 as the orange curve.

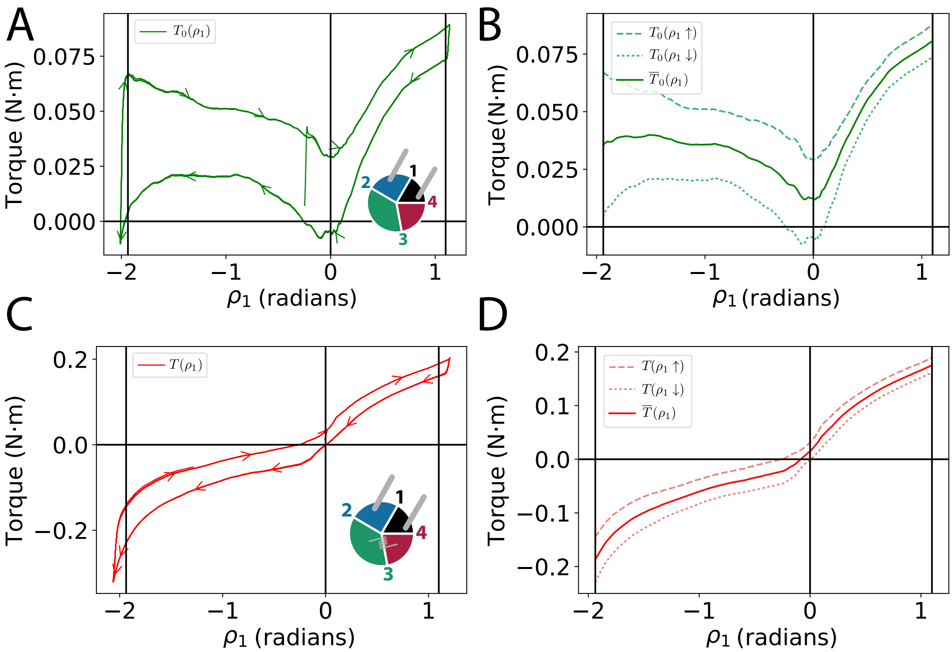

FIGURE 5.12: (A) Raw data T_0 of the the monostable branch of a $< 2\pi$ vertex, without spring attached (see inset). (B) Mean signal $\overline{T}_0$ eliminates friction but has contributions from gravity. (C) Raw data T of the monostable branch of a $< 2\pi$ vertex, *with* spring attached (see inset). (D) Mean signal $\overline{T}_0$ eliminates friction but has contributions from gravity as well as the spring.

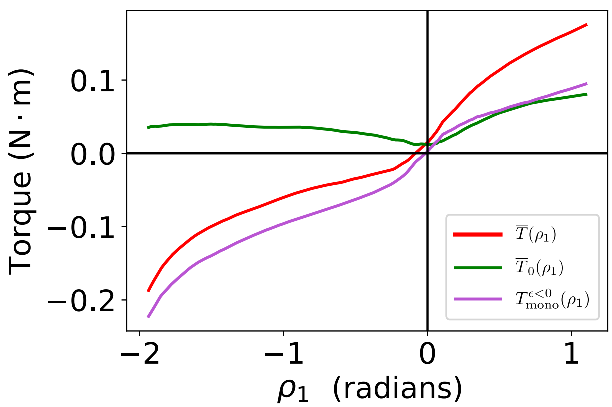

FIGURE 5.13: The difference between $\overline{T}$ (red) and $\overline{T}_0$ (green), results in the torsion signal for the monostable branch: $T^{\epsilon<0}_{\rm mono}$ (purple).

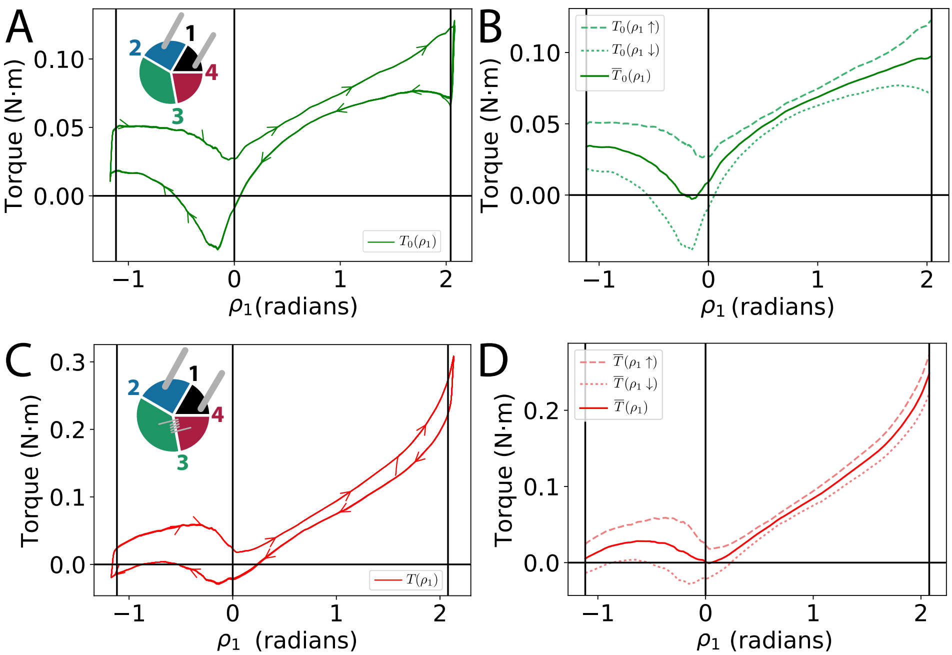

FIGURE 5.14: (A) Raw data T_0 of the the bistable branch of a $< 2\pi$ vertex, without spring attached (see inset). (B) Mean signal $\overline{T}_0$ eliminates friction but has contributions from gravity. (C) Raw data T of the bistable branch of a $< 2\pi$ vertex, *with* spring attached (see inset). (D) Mean signal $\overline{T}_0$ eliminates friction but has contributions from gravity as well as the spring.

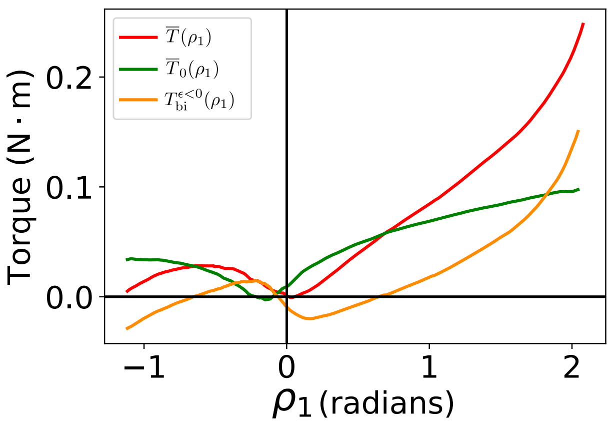

FIGURE 5.15: The difference between $\overline{T}$ (red) and $\overline{T}_0$ (green), results in the torsion signal for the bistable branch: $T_{\rm bi}^{\epsilon<0}$ (orange).

Monostable and Bistable Branch for a Saddle-like Vertex

The torque measurements for the bi- and monostable branches for the $\epsilon = \pi/60$ vertex are shown in Fig. 5.18 and Fig. 5.16 respectively. The difference with respect to the cone-like, $\epsilon = \pi/60$ vertices is that the torsional spring is now put on the ρ_1 fold, whereas the plates connected by the ρ_3 fold are clamped. The torque measurements of the monostable branch, where the vertex is 'popped through' such that $\rho_1 < 0$, is summarized in Fig. 5.17, where we show $T^{\epsilon>0}_{\rm mono}(\rho_3) = \overline{T}(\rho_3) - \overline{T}_0(\rho_3)$ in purple. The torque data of the bistable branch –where $\rho_1 > 0$– is summarized by Fig. 5.19, where the gravity corrected signal $T^{\epsilon>0}_{\rm bi}(\rho_3) = \overline{T}(\rho_3) - \overline{T}_0(\rho_3)$ is shown by the orange line.

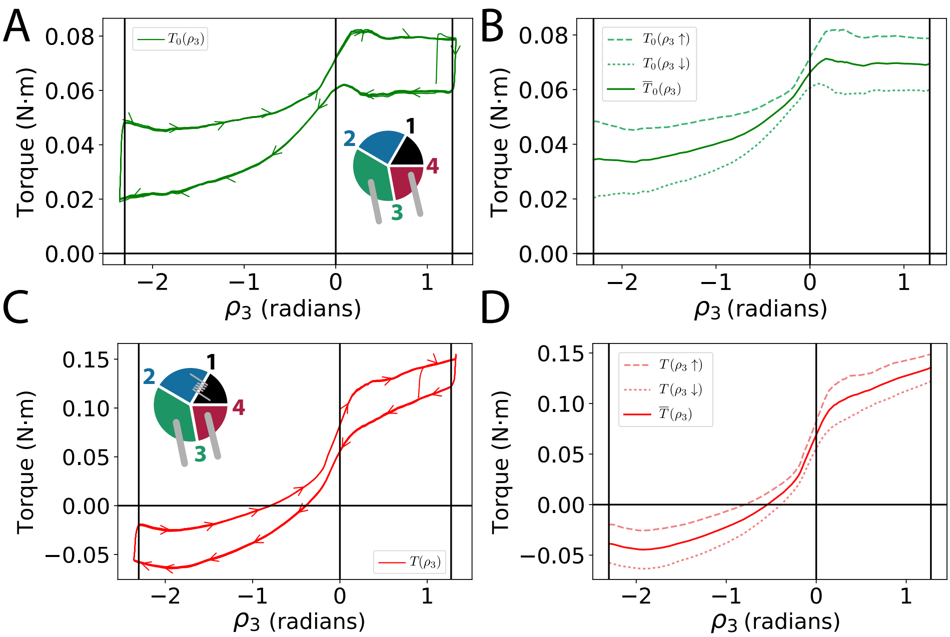

FIGURE 5.16: (A) Raw data T_0 of the monostable branch of an $\epsilon > 0$ vertex, without spring attached (see inset). (B) Mean signal $\overline{T}_0$ eliminates friction but has contributions from gravity. (C) Raw data T of the monostable branch of an $\epsilon > 0$ vertex, *with* spring attached (see inset). (D) Mean signal $\overline{T}_0$ eliminates friction but has contributions from gravity as well as the spring.

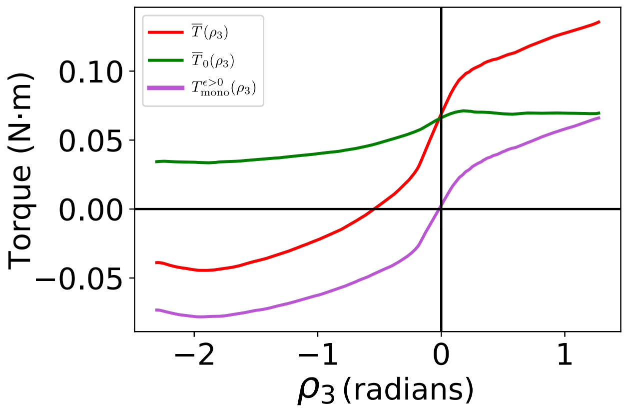

FIGURE 5.17: The difference between $\overline{T}$ (red) and $\overline{T}_0$ (green), results in the torsion signal for the monostable branch: $T^{\epsilon>0}_{\rm mono}$ (purple).

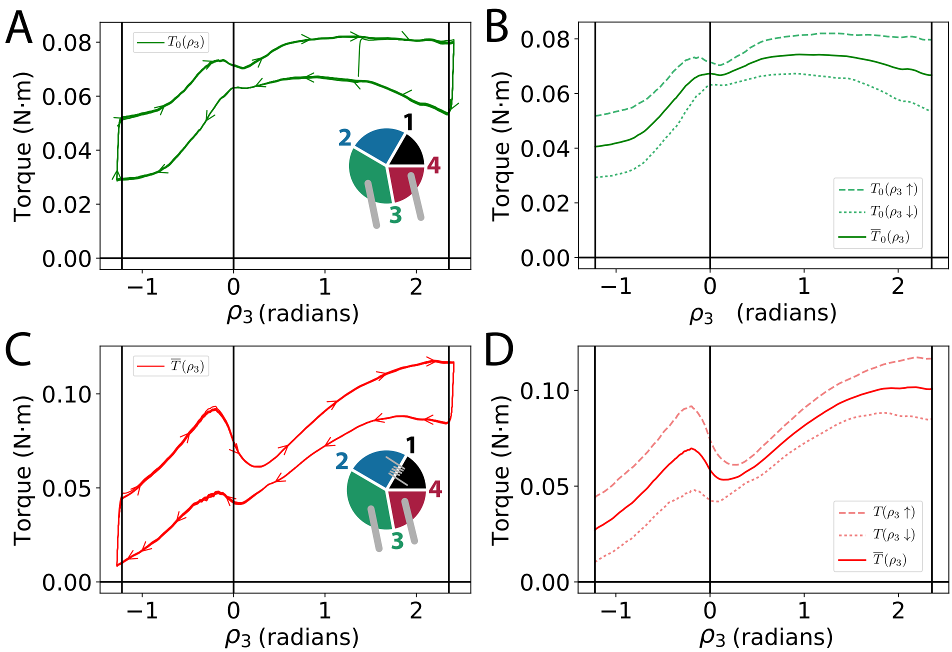

FIGURE 5.18: (A) Raw data T_0 of the bistable branch of an $\epsilon > 0$ vertex, without spring attached (see inset). (B) Mean signal $\overline{T}_0$ eliminates friction but has contributions from gravity. (C) Raw data T of the bistable branch of an $\epsilon > 0$ vertex, *with* spring attached (see inset). (D) Mean signal $\overline{T}_0$ eliminates friction but has contributions from gravity as well as the spring.

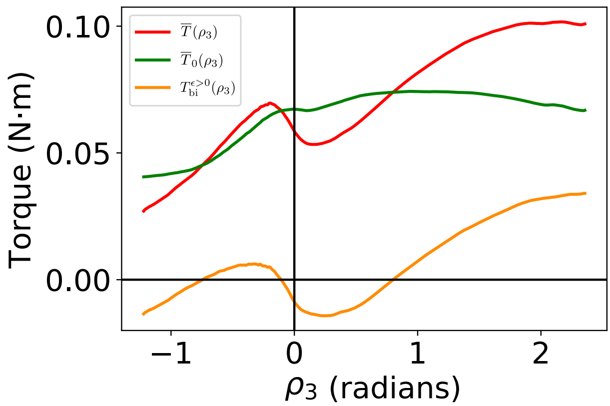

FIGURE 5.19: The difference between $\overline{T}$ (red) and $\overline{T}_0$ (green), results in the torsion signal for the monostable branch: $T_{\rm bi}^{\epsilon>0}$ (orange).

5.4.4 Experimental Energy Curves

In this section we translate our experimental data for the torque as function of fold angle to curves of the elastic energy as function of the fold angle. Subsequently we compare our experimental energy landscapes to our theoretical predictions of section 5.2.2. In addition, we experimentally characterize the energy barriers between the two folding branches, $E_{\rm pop}$. In order for the three minima of our vertices to be stable, $E_{\rm pop}$ should be larger than the energy barrier separating the two global minima on the bistable branch, $E_{\rm barrier}$, and also larger than the energy of the minimum on the monostable branch, $E_{\rm min}$. We first discuss how to extract $E_{\rm min}$ from the spring potential. After this we show how we obtain the energy curves of the mono-, and bi-stable branches from the torque data, from which we can extract $E_{\rm barrier}$. Finally, we perform an additional, linear compression experiment, which we use to characterize $E_{\rm pop}$.

Together, our data shows good agreement to our theoretical model, and a clear separation of the two folding branches and the three stable states, for cone-like as well as saddle-like vertices.

Spring Potential

In this section we extract the spring potential from our experimental data, for both the cone-like vertices (section 5.4.3), and the saddle-like vertices (section 5.4.3). In general, torque measurements can be integrated to obtain elastic energies:

$$E(\rho_i) = \int T(\rho_i)\mathrm{d}\rho. \tag{5.9}$$

The data for $T(\rho_i)$ is shown in Fig. 5.9 and Fig. 5.11. We recall that the

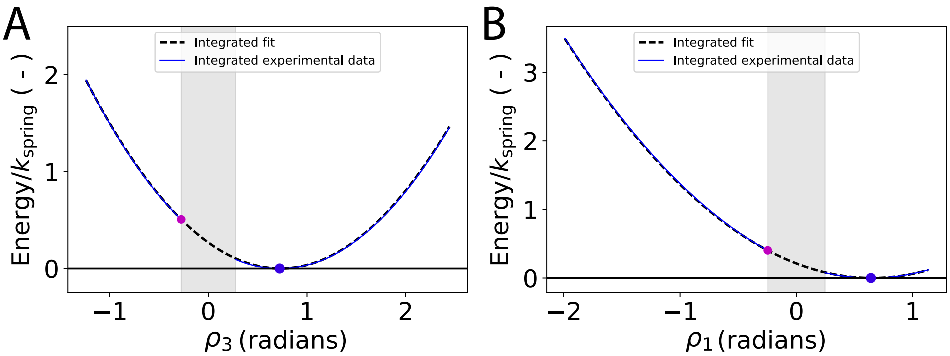

FIGURE 5.20: (A) Spring potential of the $\epsilon = -\pi/60$ vertex, extracted from the data in Fig. 5.9. (B) Spring potential of the $\epsilon = \pi/60$ vertex, extracted from the data in Fig. 5.11.

experimental data has a gap in the “forbidden" region, where ρ_3, respectively ρ_2, are pushed through the “pop-through" range where the vertex deviates from rigid-folding. Outside this gap, the torque data can be fitted well by a single linear function of the form $T = \kappa \cdot (\rho - \rho_0)$, where ρ_0 is the spring's rest angle. Piecewise integration of the energy to the left and right of this gap, and fitting the energy offsets such that (i) $E = 0$ at $\rho_{1,3} = \rho_0$ and (ii) $E(\rho)$ is continuous, we obtain the energy curves shown in Fig. 5.20. Here we non-dimensionalize our data by the torsional spring constant, κ_{spring}.

Mono, and Bistable Energy Curves

In this section we extract the mono-, and bi-stable energy curves for both the cone-, and saddle-like vertices. First, we consider the cone-like, $\epsilon = -\pi/60$ vertex. In Fig. 5.21.A the solid purple line corresponds to the experimental, dimensionless energy curve:

$$E_{\mathrm{mono}}^{\epsilon<0}(\rho_1) = \int \left[T_{\mathrm{mono}}^{\epsilon<0}(\rho_1)\right] \mathrm{d}\rho_1, \tag{5.10}$$

where $T_{\mathrm{mono}}^{\epsilon<0}(\rho_1)$ is the torque signal displayed in Fig. 5.13. The bistable, dimensionless energy curve is displayed Fig. 5.21.B as the solid orange line:

$$E_{\mathrm{bi}}^{\epsilon<0}(\rho_1) = \int \left[T_{\mathrm{bi}}^{\epsilon<0}(\rho_1)\right] \mathrm{d}\rho_1, \tag{5.11}$$

where $T_{\mathrm{bi}}^{\epsilon<0}(\rho_1)$ is the torque signal displayed in Fig. 5.15.

Second, we consider the saddle-like, $\epsilon = \pi/60$ vertex. In Fig. 5.21.C the solid purple line corresponds to the experimental, dimensionless energy curve:

$$E_{\mathrm{mono}}^{\epsilon>0}(\rho_3) = \int \left[T_{\mathrm{mono}}^{\epsilon>0}(\rho_3)\right] \mathrm{d}\rho_3, \tag{5.12}$$

where $T_{\mathrm{mono}}^{\epsilon>0}(\rho_3)$ is the torque signal displayed in Fig. 5.17. The bistable, dimensionless energy curve is displayed Fig. 5.21.D as the solid orange line:

$$E_{\mathrm{bi}}^{\epsilon>0}(\rho_3) = \int \left[T_{\mathrm{bi}}^{\epsilon>0}(\rho_3)\right] \mathrm{d}\rho_3, \tag{5.13}$$

where $T_{\mathrm{bi}}^{\epsilon>0}(\rho_3)$ is the torque signal displayed in Fig. 5.19.

The dashed lines in Fig. 5.21 indicate our theoretical predictions for the energy curves for the non-Euclidean vertices, using the appropriately determined spring potentials.

For the $\epsilon = -\pi/60$ vertex, we experimentally find that the minima B and C in Fig. 5.21.B are located at $\rho_1 \approx -0.66$ and $\rho_1 = 0.64$ respectively. Assuming a single spring located at ρ_3 with a rest angle of $0.73(1)$ rad (Fig. 5.9), theory predicts these minima to be located at $\rho_1 = \pm 0.73$ rad, which closely match the experiment. Furthermore, we find that the single minimum on the monostable branch is located at $\rho_1 \approx 0.01$ in the experimental data (Fig. 5.21.A), whereas we expect it to be located at $\rho_1 = 0.0$. While it is difficult to put a precise errorbar on our determination of the location of the minima, which is dominated by fabrication errors, play, clamping errors, and the shallowness of the minima, we estimate our errorbar to be larger than the signal, of the order of 0.1 rad.

For the $\epsilon = \pi/60$ vertex, we find that the minima E and F in Fig. 5.21.D are located at $\rho_3 \approx -0.74$ rad, and $\rho_3 \approx 0.80$ respectively. Based on theory –

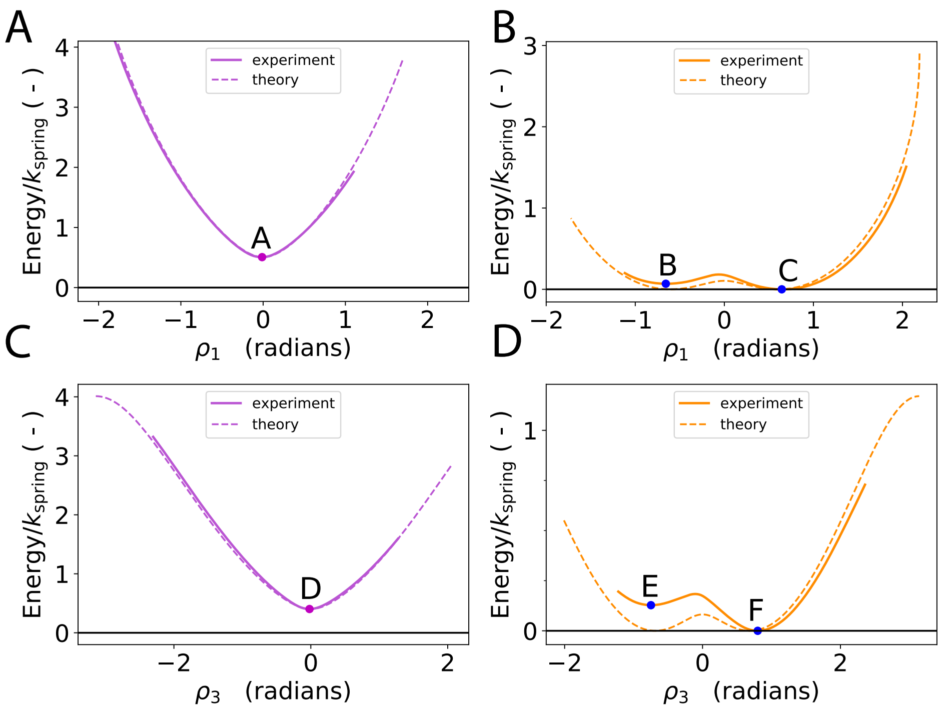

FIGURE 5.21: (A) Experimental and theoretical dimensionless energy curves for the monostable folding branch of the $\epsilon = -\pi/60$ vertex. The minimum energy is set to $E_{\text{min}} = 0.51$, corresponding to the energy of the purple point in Fig. 5.20.A. (B) Energy curves for the bistable folding branch of the $\epsilon = -\pi/60$ vertex. (C) Energy curves for the monostable folding branch of the $\epsilon = \pi/60$ vertex. Hence the minimum energy is set to $E_{\text{min}} = 0.40$, corresponding to the energy of the purple point in Fig. 5.20.B. (D) Energy curve for the bistable folding branch of the $\epsilon = \pi/60$ vertex. The letters indicating the various minima correspond those in Fig. 5.6.

assuming a single spring located at ρ_1 with a spring constant of $0.65(1)$ rad– we expect them to be located at $\rho_3 = \pm 0.69$. We suggest that the relatively large deviation of the location of the left minimum may be attributed to an offset in the torque signal of Fig. 5.19, which tilts the integrated potential shown in Fig. 5.21.D, and therefore also shifts the location of the minima. We note that the distance between the two minima is within 5% of what we expect from theory. Finally, the single minimum on the monostable branch is located at $\rho_3 \approx 0.02$ in the experimental data (Fig. 5.21.C), whereas we expect it to be located at $\rho_3 = 0.0 \pm 0.1$.

We conclude that the four experimental energy curves shown in Fig. 5.21 demonstrate that theory and experiment agree closely, as the shape of the experimental mono- and bistable branches, as well as the location of the experimental minima, closely match the dashed theoretical curves.

5.4.5 Vertex Pop-Through

In this section we characterize the pop-through behavior of our vertices. The energy barrier for pop-through, E_{pop}, is presumably set by hinge stretching and plate bending. These two effects both directly influence the peak shown in Fig. 5.9 and Fig. 5.11. In these experiments we see that the torque signal rises (drops) relatively slowly, until it hits a peak value, after which the torque suddenly drops due to the pop-through instability, resulting a in a near vertical slope. This is akin to the way the load-displacement curve of a simple von Mises truss becomes asymmetric when, instead of perfect displacement control, it is loaded with a spring, see Fig. 5.22 and p.278–p.285 of [75].

In order to quantify E_{pop}, we use a linear compression testing machine (Instron 3361) to measure the force required to flatten the vertex, without any torsional spring attached to the vertex. A schematic of our experiment is depicted in 5.22. We put our vertices on a flat surface, and measure the energy necessary to flatten it, which can be calculated from $\Delta E = \int F_z \mathrm{d}z$, where F_z is the force exerted by the compression tester. When loading the vertex, F_z will rise to a maximum value $F_z = F_{z,\text{peak}}$, starting from $F_z = 0$ (Fig. 5.22.A,B). After this, F_z will drop back to $F_z = 0$ for the fully flattened vertex. On the contrary, E will monotonically increase, and we take the maximum value of E for the fully compressed vertex as the pop-through energy barrier, E_{pop}.

The setup that we use in the vertical Instron testing machine consist of single $\epsilon \approx -0.052$, cone-like vertex, with geometric parameters identical to the one used for the experiments in section 5.4. To this vertex we glue 4 truncated spheres: three to the bottom, at approximately 120° apart along the periphery of the vertex, and one to the top, near the center of the vertex – see Fig. 5.23.A. The vertex is then placed in between two parallel circular plates with a diameter of 20.0 cm, see Fig. 5.23.B. This setup creates a well defined contact on the top and the bottom, and avoids the need for any

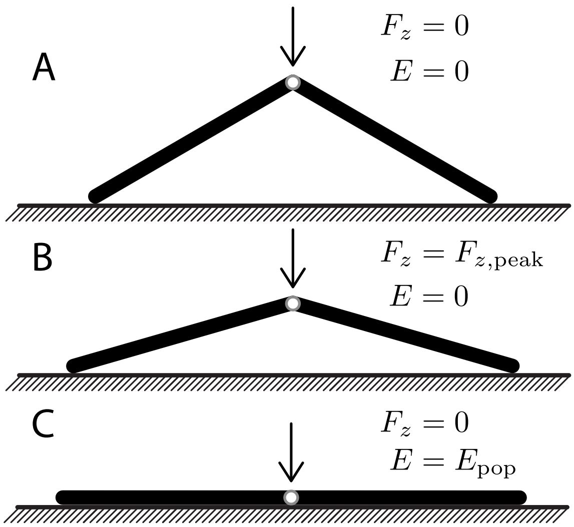

FIGURE 5.22: Side-view schematic of the setup used to measure the energy necessary to pop-through the vertex, E_{pop}. (A) Start of the experiment: the vertex is uncompressed, $E = 0$, and $F_z = 0$. (B) Approximately halfway the experiment, the force exerted in the z direction will hit a maximum F_z, $E > 0$. (C) The vertex is fully compressed. Vertically exerted force is once again $F_z = 0$, whereas the elastic energy is now maximal, $E = E_{\mathrm{pop}}$.

precise parallel alignment of the top and bottom plate. Lastly, the spheres as well as the aluminum plates are all coated with silicone grease in order to minimize friction.

A similar setup is used for the $\epsilon \approx 0.052$, saddle like vertex. However, as the pop-through transition in this case transforms the vertex from one saddle configuration to another, pushing on the vertex on a single point near the center does not pop the vertex through. Therefore, we use a a different arrangement of spheres: two spheres are glued to the bottom of the vertex, on opposite sides, and two on the top, also on opposite sides, where the two pairs approximately form a cross (Fig. 5.23.C). A picture of this configuration is shown in Fig. 5.23.D.

The result of the measurement for the $\epsilon \approx -0.052$ vertex is shown in Fig. 5.24.A. The measurement protocol consists of lowering the top plate until it is about to make contact with the top sphere, as depicted in Fig. 5.23.B. We then impose an up and down sweep of the z-displacement, Δz, where we use a strain rate of 0.1 mm/s, and a maximum Δz of 1.6 mm

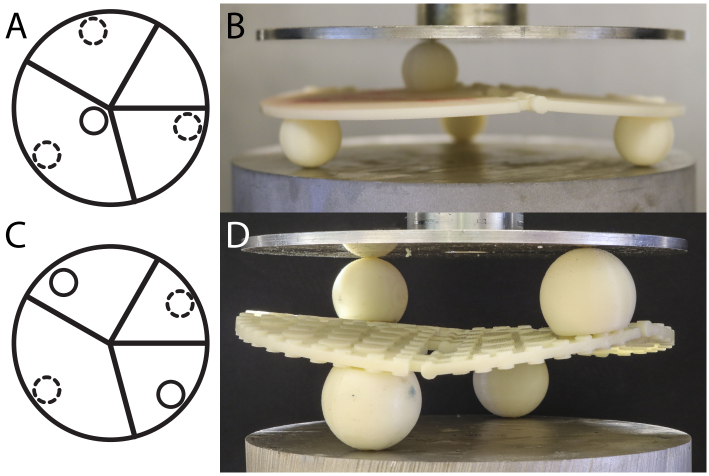

FIGURE 5.23: (A) Top-view schematic of the $\epsilon < 0$, hat-like vertex, where the position of the attached spheres is indicated by the circles; dashed lines indicate the spheres are attached to the underside of the vertex. (B) Side view of the $\epsilon < 0$ in our compression setup. (C) Top-view schematic of the $\epsilon > 0$, saddle-like vertex, where the position of the attached spheres is indicated by the circles; dashed lines indicate the spheres are attached to the underside of the vertex. (D) Side view of the $\epsilon > 0$ vertex in our compression setup.

(positive Δz means pushing down). This maximum is increased by 1.0 mm every second cycle to $\Delta z = 2.6, 3.6, 4.6, 5.6$ mm, and finally $\Delta Z = 6.6$ mm. On the last cycle we see that the vertex pops through, at $\Delta z \approx 6.28$ mm. We see that from $\Delta z \lesssim 3$ mm, F_z increases to a peak value, which we determine to be $F_{z,\text{peak}} = 19.5 \pm 0.5$ N, obtained by taking the average maximum over seven up sweeps – the error bar represents the standard deviation of seven maximum values. After hitting this peak value, F_z monotonically decreases all the way down to $F_z = 0$; the top plate staying in contact all the way till the pop-through point. The amount of work necessary to pop-through the vertex can now be calculated by integrating the signal of Fig. 5.24.A, as we have done in Fig. 5.24.B, and we find a value of $W_{\text{pop}} = 0.065$ J. Finally, we note the large discrepancy between F_z for the upward sweeps, and the downward sweeps. We attribute this discrepancy to friction in the hinges, which we also witnessed in our torsion experiments (section 5.4). Hence, the amount of work is not equal to the maximum elastic energy stored in the deformed configuration, E_{pop}.

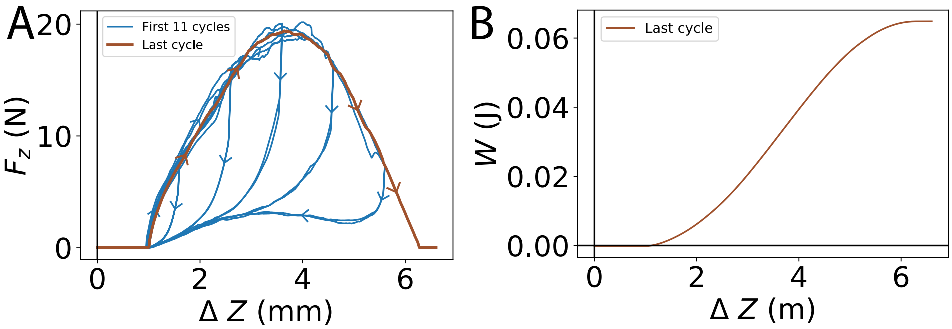

FIGURE 5.24: (A) Data of the compression experiment depicted in Fig. 5.23, for a $\epsilon \approx -0.052$ rad vertex. Top plate makes contact with the vertex $\Delta z = 1.0$ mm, and is further compressed until $\Delta z = 1.6$ mm using up an down sweeps of Δz, where the maximum Δz is increased by 1.0 mm every other sweep. The last sweep (brown) reaches a maximum of $\Delta z = 6.6$ mm, where we witness a pop-through event at $\Delta z = 6.275$ mm. (B) Integrated signal of (A); we find $W_{\text{pop}} = 0.065$ J.

The result of the measurement for the $\epsilon \approx 0.052$ vertex is shown in Fig. 5.25.A. In this experiment the top plate makes contact with the vertex at a z-displacement of around $\Delta z = 1.0$ mm, and is further compressed until $\Delta z = 6.2$ mm, which is just before the pop-through point, for three up an down sweeps. On next compression cycle we increase the maximum z-displacement to $\Delta z = 10$ mm, and we witness a pop-through event at $\Delta z = 7.37$ mm. The sudden drop in F_z at this point is where the vertex pops through, and the top plate loses contact. The fact this happens before F_z drops to zero, probably indicates the vertex is not perfectly flattened, which would require precise alignment of the four attached spheres (unlike in the $\epsilon > 0$ case, where the four contacts are self-aligning). The average peak load found in this case is $F_{z,\text{peak}} = 15.5 \pm 0.1$ N, which was determined by taking the average of the peak load over four up sweeps, and likewise for the errorbar, which corresponds to the standard deviation of these four peak loads. This peak load is of the same order as the peak load found for the $\epsilon \approx 0.052$ vertex. The integrated signal is equivalent to the amount of work necessary to pop the vertex through, and is displayed in Fig. 5.25.C. The 'pop-through work' is calculated from the total area under the curve in Fig. 5.25.A, which results in $W_{\text{pop}} = 0.072$ J, which is approximately 10% higher than the W_{pop} value found for the $\epsilon > 0$ case. Our data clearly shows that this barrier is significantly larger than the energy scales on a single branch; hence once popped, the vertex will stay on one of these branches. We also note that W_{pop} for the $\epsilon > 0$ and $\epsilon < 0$ vertices are similar. This suggests that hinge stretching constitutes the main deviation from rigid folding; if instead plate bending would dominate, $\epsilon > 0$ vertices can easily be popped, but $\epsilon < 0$ vertices not[2]. Finally, the monotonous increase of the "in plane" forces, while F_z goes to zero, suggests that frictional forces must be important, even if the friction coefficient is small.

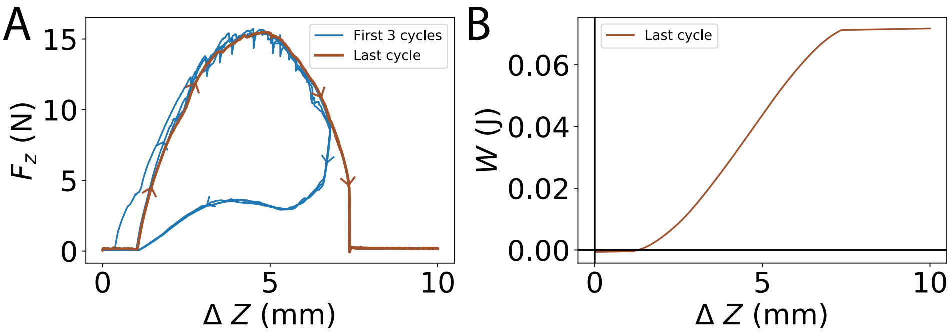

FIGURE 5.25: (A) Data of the compression experiment depicted in Fig. 5.23, for an $\epsilon \approx 0.052$ vertex. Top plate makes contact with the vertex at $\Delta z = 1.0$ mm, and is further compressed until a maximum of $\Delta z = 6.2$ mm using a triangular waveform, for 3 cycles. On the last cycle Δz is increased to $\Delta z = 10.0$ mm, where we witness a pop-through event at $\Delta z = 7.37$ mm. (B) Integrated signal of (A): we find $W_{\text{pop}} = 0.072$ J.

In order to determine how W_{pop} depends on the angular surplus (or deficit), we 3D printed four additional $\epsilon < 0$ vertices, for $\epsilon = -\pi/120 \approx -0.025$ rad, $\epsilon = -\pi/72 \approx 0.044$ rad, $\epsilon = -\pi/45 \approx -0.070$ rad, and $\epsilon = -\pi/30 \approx -0.105$ rad. The $\epsilon \approx -0.026$ rad vertex has a negligible bump, which in particular is not enough to support the vertex's weight when put in a 'cone up' configuration on a flat surface – this is likely due to small but finite play of the hinges. On the other extreme, repeatedly popping through the $\epsilon \approx -0.105$ rad vertex breaks one of the outermost hinges of the vertex within ten cycles, indicating the stresses put on these hinges is beyond the yield stress of the material (ABS). The results of the compression tests of the remaining three vertices: $\epsilon \approx \{-0.044, -0.052, -0.070\}$, are shown in Fig. 5.26.A. The curves here correspond to the last compression cycle of

[2]This can readily be demonstrated by making non-Euclidean vertices out of paper, where the 'pop-through' transition is facilitated by bending the paper.

each test, where the brown curve in Fig. 5.26.A corresponds to the brown curve in Fig. 5.24.A. To characterize the increase in bump size as a function of surplus angle ϵ, we integrate each curve to find the energy underneath each curve, and plot this value as function of ϵ, as shown in Fig. 5.26.B. The points suggest there is a linear relationship between the amount of work, W_{pop}, and the surplus angle, ϵ. A fit of the form $Wpop = a \cdot \epsilon + b$ is displayed in Fig. 5.26.B as the black line. We find $a = -3.34\ J/\text{rad}$ and $b = -0.109\ J$, which translates to a cut-off point of $\epsilon \approx -0.033$ rad. This is consistent with the observation that the $\epsilon \approx -0.026$ rad vertex has a negligible barrier. We note that this relationship is specific to this geometry and vertex size. Most hinge stretching and bending takes place around the periphery of the vertex, and the maximum stresses exerted on the hinges will decrease if we print a vertex with a smaller radius, but otherwise identical geometric parameters. We do expect however, to find a roughly similar relationship between W_{pop} and ϵ for $\epsilon > 0$ vertices, as W_{pop} for the $\epsilon = -0.052$ and $\epsilon = +0.052$ vertices differs by only 10%.

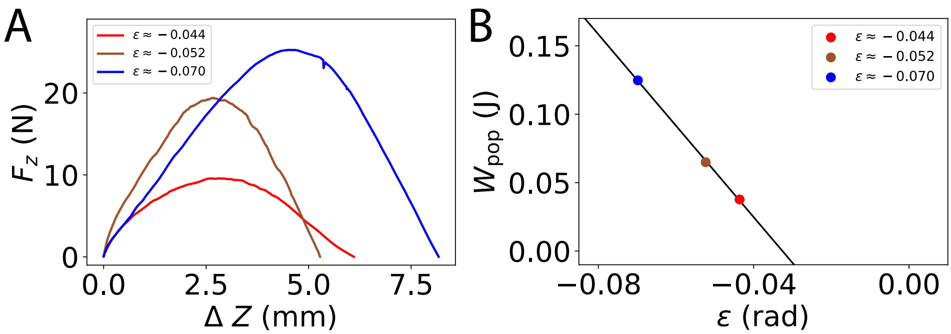

FIGURE 5.26: (A) Last compression cycle of three different vertices, with $\epsilon \approx -0.044$, $\epsilon \approx -0.052$, and $\epsilon \approx -0.070$. The brown, $\epsilon \approx 0.052$ curve corresponds to the brown curve displayed in Fig. 5.24.A. (B) W_{pop} found by integrating the three curves in (A), black line indicates a linear fit (see text).

Finally, we observe that W_{pop}, E_{min} and E_{barrier} can all be expressed in terms of dimensionless units, e.g:

$$\tilde{W}_{\text{pop}} = W_{\text{pop}}/k_{\text{spring}}, \tag{5.14}$$

which yields $\tilde{W}_{\text{pop}} \approx 1.43$ for the $\epsilon \approx -0.052$ vertex , and $\tilde{W}_{\text{pop}} \approx 1.57$ for the $\epsilon \approx 0.052$ vertex. From Fig. 5.21 we can see that $\tilde{E}_{\text{min}} \ll \tilde{W}_{\text{pop}}$ and

$\tilde{E}_{\text{barrier}} < \tilde{W}_{\text{pop}}$, which is consistent with our observation that both vertices are tri-stable.

5.5 Conclusion

In this chapter we have shown how to create experimentally robust *tristable vertex*. We use weakly non-flat 4-vertices that exhibit two folding branches that are separated by a finite energy barrier, controlled by a non-rigid "pop-through transition. By dressing one of the folds with a torsional spring, we can turn one of the two folding branches into a bistable branch, thereby creating tristable vertices. The fact that this same mechanism works for both cone-like ($\epsilon < 0$) as well as saddle-like ($\epsilon > 0$) vertices opens up the possibility to create corrugated sheets composed out of tristable non-flat vertices, for which we need both saddle-like and cone-like vertices.